PCCP

Density functional study of phase stabilities and Raman spectra of Yb_2O_3, Yb_2SiO_5 and $Yb_2Si_2O_7$ under pressure

Journal:	*Physical Chemistry Chemical Physics*
Manuscript ID	CP-ART-04-2018-002497.R1
Article Type:	Paper
Date Submitted by the Author:	18-May-2018

Complete List of Authors:	Ogawa, Takafumi; Japan Fine Ceramics Center, Nanostructures Research Laboratory Otani, Noriko; Japan Fine Ceramics Center, Nanostructures Research Laboratory Yokoi, Taishi; Japan Fine Ceramics Center, Materials Research and Development Laboratory Fisher, Craig; Japan Fine Ceramics Center, Nanostructures Research Laboratory Kuwabara, Akihide; Japan Fine Ceramics Center, Nanostructures Research Laboratory; National Institute for Materials Science, Center for Materials Research by Information Integration Moriwake, Hiroki; Japan Fine Ceramics Center, Nanostructures Research Laboratory; National Institute for Materials Science, Center for Materials Research by Information Integration Yoshiya, Masato; Osaka University, Department of Adaptive Machine Systems; Japan Fine Ceramics Center, Nanostructures Research Laboratory Kitaoka, Satoshi; Japan Fine Ceramics Ceter, Materials Research and Development Laboratory Takata, Masasuke; Japan Fine Ceramics Center, Nanostructures Research Laboratory; Japan Fine Ceramics Ceter, Materials Research and Development Laboratory

PCCP

ARTICLE TYPE

Cite this: DOI: 10.1039/xxxxxxxxxx

Density functional study of phase stabilities and Raman spectra of Yb_2O_3, Yb_2SiO_5 and $Yb_2Si_2O_7$ under pressure†

Takafumi Ogawa,*[a] Noriko Otani,[a] Taishi Yokoi,[b] Craig A. J. Fisher,[a] Akihide Kuwabara,[a,c] Hiroki Moriwake,[a,c] Masato Yoshiya,[a,d] Satoshi Kitaoka,[b] and Masasuke Takata[a,b]

Received Date
Accepted Date

DOI: 10.1039/xxxxxxxxxx

www.rsc.org/journalname

Phase stabilities and Raman spectra of Yb_2O_3, Yb_2SiO_5 and $Yb_2Si_2O_7$ under hydrostatic pressure are investigated using density functional theory calculations. Calculated energies of polymorphs of each compound show that the stable phases at zero pressure, viz., C-type Yb_2O_3, X_2-Yb_2SiO_5 and β-$Yb_2Si_2O_7$, exhibit a pressure-induced phase transition as compressive pressure increases, which is consistent with available experimental data. The theoretical Raman spectra at zero pressure are in good agreement with experimental results for the stable phases and can be used to identify each polymorph. Although the calculated pressure dependence of Raman peak positions of C-type Yb_2O_3 is overestimated compared to available experimental data, piezospectroscopic coefficients extracted from Raman peaks of X_2-Yb_2SiO_5 and β-$Yb_2Si_2O_7$ suggests that Raman spectroscopy can be used to measure stresses and strains in the Yb silicates. Normal mode analyses reveal that characteristic Raman peaks of Yb silicates at frequencies above 600 cm^{-1} are strongly associated with vibrations of Si-O bonds in Si_xO_y tetrahedral units.

1 Introduction

When used in high-temperature applications such as advanced aircraft engines, SiC-based ceramic-matrix composites (CMCs) require environmental barrier coatings (EBCs)[1,2] to prevent the base materials from reacting with water vapor to form silicon hydroxide gases such as $Si(OH)_4$.[3,4] Both rare-earth monosilicates, R_2SiO_5, and disilicates, $R_2Si_2O_7$, where R = rare earth elements, constitute families of candidate EBC materials by virtue not only of their stability under volatilizing environments but also of having a coefficient of thermal expansion (CTE) close to that of the underlying CMC.[5–8] Mechanical, morphological and chemical changes of coated and single-phase samples under high-temperature water vapour have been reported for R = Sc, Y, Gd, Er, Yb, and Lu (see, e.g., the recent review by Xu *et al.*[8] and references therein). Notably, Yb_2SiO_5[9] and $Yb_2Si_2O_7$[10] exhibit high phase stability with no structural phase transition at high temperature and have been the most widely investigated.[5,6,11–17]

Recently, Richards *et al.* examined degradation mechanisms during thermal cycling of a multilayered EBC consisting of Yb_2SiO_5, mullite ($Al_6Si_2O_{13}$) and Si formed by atmospheric plasma spraying.[14,16] In this configuration, mullite and Si layers act as an oxidation barrier and bonding layer, respectively, for the underlying CMC.[3,5] Their experiments showed that cracks form and propagate in the top coat owing to the CTE mismatch between Yb_2SiO_5 and the underlying ceramics. This is followed by thermal growth of SiO_2, known as a thermally grown oxide or TGO, at the interface between mullite and Si layers. Because cristobalites in the TGO layer undergo phase transitions with large volume changes, these processes eventually induce a critical spallation of the EBC. Although $Yb_2Si_2O_7$ has a more suitable CTE for the CMC substrates and Si bonding layer compared to Yb_2SiO_5, incongruent vapourization of the disilicates to the monosilicates in high-temperature water vapour environments raises concerns about delamination by thermal contraction of Yb_2SiO_5 as temperature decreases.[15] In order to improve performance and durability of such EBCs, phase compositions and structures, as well as residual stresses, in the component materials need to be closely monitored and controlled.

Several methods for measuring residual stresses or strains in solid-state materials non-destructively have been actively devel-

[a] Nanostructures Research Laboratory, Japan Fine Ceramics Center, Nagoya 456-8587, Japan. E-mail: t_ogawa@jfcc.or.jp
[b] Materials Research and Development Laboratory, Japan Fine Ceramics Center, Nagoya 456-8587, Japan.
[c] Center for Materials Research by Information Integration, National Institute for Materials Science, Tsukuba 305-0047, Japan
[d] Department of Adaptive Machine Systems, Osaka University, Osaka 565-0871, Japan
† Electronic Supplementary Information (ESI) available: Pressure dependences of Raman spectra and vibrational mode analyses. See DOI: 10.1039/cXCP00000x/

oped utilizing optical (including lasers and synchrotron X-rays), acoustic, neutron, and electronic probes.[18,19] For example, fluorescence microscopy of Cr impurities in α-Al_2O_3,[20–22] Raman spectroscopy of yttria-stabilized zirconia (YSZ),[23,24] and synchrotron X-ray diffraction of entire components[25,26] have been used to characterise stress distributions and investigate fatigue mechanisms in thermal barrier coatings (TBCs). Improving the spatial resolution is, therefore, an important goal, as each method has different measurement ranges, as summarised by Michaels and Cook.[22] Raman microscopy is a useful technique because of its relatively easy operation and spatial resolution on the order of microns. Although Raman microscopy is useful for characterising EBC materials, to the best of our knowledge, with the exception of pressure-dependent Raman spectra of single-crystal $Lu_{1.8}Y_{0.2}SiO_5$,[27] there are no previous reports on Raman spectra of R_2SiO_5 and $R_2Si_2O_7$ under axial stresses or hydrostatic pressures.

Results of measurements of Raman spectra as a function of stress can vary depending on the sample preparation method or measurement technique, as seen in the case of YSZ.[28] Theoretical prediction of these properties is an alternative approach to evaluate the usefulness of Raman microscopy to measure stress distributions in EBC components. Density functional theory (DFT) provides a theoretical method for generating peak positions and their intensities in Raman spectra of single crystals.[29,30] Combining this type of calculation with calculations of systems under external pressure can reveal the pressure dependence of Raman spectra quantitatively. Note that Raman spectra calculated by DFT at zero Kelvin are similar to those at room temperature, the temperature at which residual stress measurements after thermal cycling are typically performed.

In this study, using DFT calculations we investigated the dependences of phase stability and Raman spectra of Yb silicates (Yb_2SiO_5 and $Yb_2Si_2O_7$), two of the most promising EBC materials,[6,11–13,15,17] on hydrostatic pressure. We also investigated Yb sesquioxide, Yb_2O_3, which has been observed as a secondary phase or decomposition phase in Yb silicate coatings.[17,31] Since many more experimental and theoretical studies have been carried out on Yb_2O_3 compared to the structurally more complex Yb silicates, a systematic study including Yb_2O_3 helps verify the validity of the methodology we use here to determine structure-dependent properties. In the case of the silicates, we compare theoretical Raman spectra at zero pressure with experimental spectra obtained using polycrystalline samples under atmospheric conditions.

2 Calculation and experimental methods

All DFT calculations were performed using the projector augmented wave (PAW) method[32] with the Perdew-Burrk-Ernzerhof generalized gradient approximation,[33] as implemented in the VASP code.[34–36] In the PAW potentials, $5s^25p^66s^2$, $3s^23p^2$, and $2s^22p^4$ were treated as valence electrons for Yb, Si and O atoms, respectively, where $4f$ electrons of Yb ions were frozen by assuming a Yb^{3+} ionic state. Although the $4f$ electrons can be treated explicitly by more sophisticated calculation methods such as GW_0[37] and DFT+U[38,39] for electronic and optical properties the structural and vibrational properties are expected to be represented adequately by the Yb^{3+} potential. A cutoff energy for plane-wave bases of 550 eV was used in all calculations. Summation over the Brillouin zone was performed based on the Monkhorst-Pack method.[40] Structural optimisations were performed for all forces to achieve below 0.01 eV/Å. Standard formation enthalpies of each compound, ΔH_f, were calculated by subtracting optimised energies of Yb metal with an fcc lattice and an O_2 molecule from that of the target compound. Bulk moduli were calculated from the relation between volume and pressure using the third-order Birch-Murnaghan equation of state.[41,42] We calculated the phonon density of states of each compound using the Phonopy code.[43]

Raman intensity (activity) can be calculated using third-order energy perturbation with regard to normal mode vectors at the Γ point and electric fields.[29,30,44] We calculated Raman intensities using the finite displacement method implemented in the "vasp_raman.py" script which uses the VASP code as a back-end.[45] Zone-center modes and dielectric constants were calculated according to density functional perturbation theory (DFPT).[46] All Raman intensities were broadened by 7.0 cm^{-1} wide Lorentzians. Irreducible representations (or symmetry labels) of zone-centre modes were identified using the Phonopy code.[43]

Sample preparation and Raman spectroscopy measurements of polycrystalline Yb_2SiO_5 and $Yb_2Si_2O_7$ were performed in the same matter as described in our previous report.[47] Raw powders were synthesized using ultrasonic spray pyrolysis starting from silica sol (ST-OXS, Nissan Chemical Industries, Ltd.) and $Yb(NO_3)_3 \cdot xH_2O$ (99.9% purity, Nippon Yttrium Co., Ltd) in appropriate molar ratios. Green powders were calcined for 2 h in air at 1573 K for Yb_2SiO_5 and 1673 K for $Yb_2Si_2O_7$, and then ground by jet milling. Yb_2SiO_5 powders were pressed uniaxially in a mold at 25 MPa and $Yb_2Si_2O_7$ powders at 20 MPa, before densified by cold isostatic pressing at 250 MPa. Yb_2SiO_5 samples were sintered in air at 1873 K for 20 h and $Yb_2Si_2O_7$ samples at 1773 K for 5 h. Synthesized samples were confirmed to be X_2-Yb_2SiO_5 and β-$Yb_2Si_2O_7$ by X-ray diffraction. Raman spectra of the two phases were obtained using a JASCO NSR-7100 spectrometer equipped with an Nd:YVO_4 laser of wavelength 532 nm.

In this study, we focussed on the well-defined peaks of each spectrum whose positions could be determined accurately by interpolation without needing to perform complex decompositions. Comparison between calculated and experimental spectra under ambient conditions was used to validate the simulation methodology so that changes in Raman spectra of the three materials as a function of pressure could be predicted.

3 Results

3.1 Yb_2O_3

Bulk properties

There are three known polymorphs of R_2O_3 stable below 2000 K, viz., hexagonal A-, monoclinic B- and cubic C-type structures belonging to space groups $P\bar{3}m1$, $C2/m$ and $Ia\bar{3}$, respectively.[48,49] In the case of R = Yb, although C-type Yb_2O_3 is the most stable

Table 1 Lattice constants, bulk moduli (B_0) and standard formation enthalpies (ΔH_f) of Yb_2O_3 at zero pressure.

	Calc.	Exp.
C-type		
a [Å]	10.416	10.432[a]
B_0 [GPa]	153.62	144;[b] 156;[c] 181[d]
ΔH_f [kJ/mol]	-1803.57	-1814.5±6.0[e]
B-type		
a [Å]	13.823	13.73[f]
b [Å]	3.410	3.425[f]
c [Å]	8.459	8.452[f]
β [°]	100.43	100.17[f]
B_0 [GPa]	158.71	
ΔH_f [kJ/mol]	-1777.38	
A-type		
a [Å]	3.587	
c [Å]	5.786	
B_0 [GPa]	150.19	
ΔH_f [kJ/mol]	-1761.41	

[a] Saiki *et al.* [52] [b] Powell *et al.* [53]
[c] Yusa *et al.* [54] [d] Meyer *et al.* [55]
[e] Konings *et al.* [56], Huber *et al.* [57], Cordfunke and Konings [58] [f] Hoekstra [51]

over a wide temperature range under ambient pressure, B-type Yb_2O_3 is stabilized at higher pressures.[50,51]

Table 1 lists calculated bulk properties of Yb_2O_3 at zero pressure in comparison with available experimental data. The calculated lattice constants of C- and B-type Yb_2O_3 are close to the experimental values, with differences less than 1%. The obtained bulk modulus of C-type Yb_2O_3 falls within the experimental range from 144 to 181 GPa[53–55] and the range of reported calculations from 144.5 to 161.6 GPa[59]. Such scatter in the experimental data may be attributed to differences in samples such as pore sizes and distributions,[53,60] as observed for other R_2O_3 cases such as Ho_2O_3 and Er_2O_3.[59] Table 1 shows that the calculated ΔH_f of the most stable C-type phase is comparable to the experimental value. The difference in ΔH_f between C- and B-type Yb_2O_3 is 26.19 kJ/mol, which is slightly larger than the transition enthalpy of 15.38 kJ/mol obtained from experiments.[49,51] The difference in ΔH_f between B- and A-type Yb_2O_3 of 15.97 kJ/mol is also larger than the experimental transition enthalpy of 9.69 kJ/mol,[49] but both these values from calculations or experiments are about 60% lower compared to differences between C- and B-type Yb_2O_3.

Figure 1 shows plots of the pressure dependence of volume and differences in enthalpies of the three forms of Yb_2O_3. The similar curves for different phases of Yb_2O_3 in Fig. 1(a) result in similar bulk moduli in Table 1. B' in the Birch-Murnaghan equation of state was calculated to be 4.23 for C-type Yb_2O_3, which is comparable to previous DFT results,[59] but lower than the experimental value of 7.3.[55]

Figure 1(b) reveals two structural phase transitions from C- to B-type phases at 8.0 GPa ($P_{C\to B}$) and from B- to A-type phases at 27.5 GPa ($P_{B\to A}$), where $P_{X\to Y}$ means the transition pressure from X to Y phases. In Table 2, the calculated transition pressures are compared with available literature data. Although such transition pressures are difficult to determine precisely in experiments because two or three phases can coexist over a wide pressure range spanning the transition, the transition pressure extracted here is the pressure at which a new phase appears during compression. The listed experimental data are limited to those of measurements at room or lower temperatures because increases in temperature lower the critical pressure.[49]

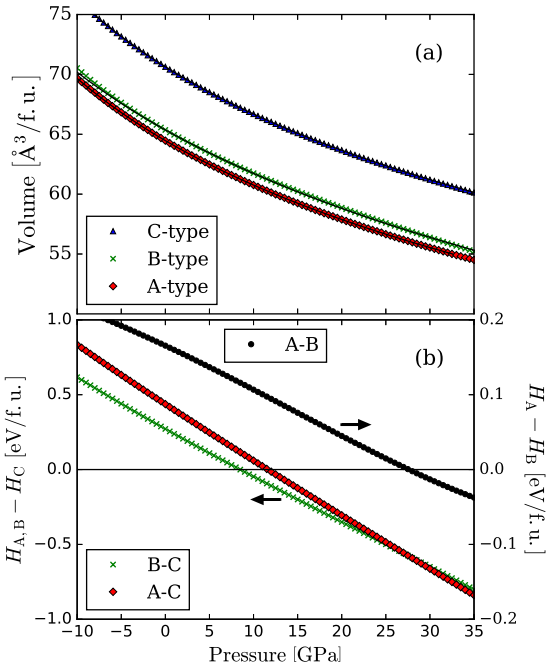

Fig. 1 Pressure dependence of (a) volume per formula unit (f.u.) of C-, B- and A-type Yb_2O_3 and (b) differences in enthalpy per formula unit of the three polymorphs.

The calculated sequence of phase transitions from the C-type to A-type via the B-type is consistent with experimental results by Yusa *et al.*[54] and Lonappan,[61] and $P_{C\to B}$ and $P_{B\to A}$ are near to those reported by Yusa *et al.*.[54] In experiments by Meyer *et al.*,[55] the B→A transition was not observed up to 25 GPa, meaning $P_{B\to A} > 25$ GPa, consistent with our results and those of Lonappan.[61]

Pandey *et al.* characterized the C→A transition from Raman spectra.[62] This direct transition may be a result of studying crystals on the order of 100 nm in size, because nanostructuring effects can induce distinct behaviour to that of bulk crystals.[63] As reported by McClure,[64] X-ray peaks of the three coexisting phases could not be easily decomposed, suggesting that the phase transformation depends on sample preparation. Direct C→A transitions from DFT calculations have been reported by Richard *et al.*;[59] they obtained a value for $P_{C\to A}$ comparable to our results and thos of Pandey *et al.*[62], as shown in Table 2.

Raman spectra

The calculated Raman spectrum of C-type Yb_2O_3 at zero pressure is plotted in Fig. 2(a) and the extracted peak positions are compared with experimental data[62,65] in Table 3. From factor group analysis for the T_h^7 point group of C-type Yb_2O_3, Raman active modes belong to $\Gamma = 4A_g + 4E_g + 14T_g$.[66] The Raman spectrum exhibits a characteristic strong peak with T_g symmetry at

Table 2 Transition pressures in units of GPa for structural transitions between C-, B- and A-type Yb_2O_3 according to eight different studies.

	$P_{C\to B}$	$P_{B\to A}$	$P_{C\to A}$
DFT (GGA)[a]	8.0	27.5	11.5
Energy dispersive XRD[b]	$\sim$ 13		
Angle dispersive XRD[c]	$\sim$ 15.9	$\sim$ 19.6	
Raman spectroscopy[d]	$\sim$12	$\sim$ 26	
Raman spectroscopy[e]			$\sim$11.3
Angle dispersive XRD[f]	($\sim$ 17)		($\sim$ 17)
DFT (LDA)[g]			7.5
DFT (WC-GGA)[g]			9.1

[a] This work [b] Meyer *et al.* [55] [c] Yusa *et al.* [54] [d] Lonappan [61] [e] Pandey *et al.* [62] [f] McClure [64] [g] Richard *et al.* [59]

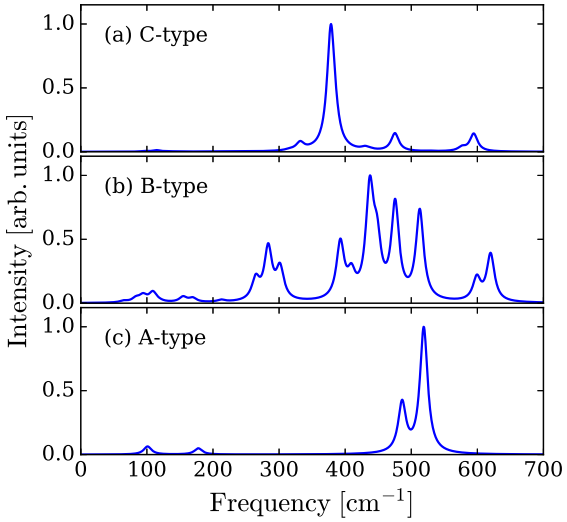

Fig. 2 Calculated Raman spectra of (a) C-, (b) B- and (c) A-type Yb_2O_3.

around 380 cm^{-1}. Although this peak corresponds to the peak at 360 cm^{-1} in experimental spectra, the symmetry label assigned to this peak in many experimental reports is $T_g + A_g$ rather than T_g. These previous reports seem to base their assignments on the work by Schaack and Koningstein,[65] in which symmetry labels for Yb_2O_3 were assumed to be the same as for Y_2O_3. Although there have been a number of Raman studies of C-type R_2O_3, polarized Raman spectra of single crystals have only been reported for Sc_2O_3 [67] and Y_2O_3,[65,68] as noted recently by Abrashev *et al.*.[69] Yb_2O_3 and Eu_2O_3 are expected to deviate from the trend established for other sesquioxides,[70] and anomalous softening of Eu_2O_3 has recently been confirmed.[69] The symmetry of the strongest peak of Yb_2O_3, therefore, is likely to be T_g.

Calculated Raman spectra of B- and A-type Yb_2O_3 are plotted in Figs. 2(b) and 2(c), respectively. The shapes of these spectra are different to that of C-type Yb_2O_3, indicating that the structure of Yb_2O_3 at high pressure can be readily identified from the experimental Raman spectra. In the experimental results reported by Lonappan [61] and Pandey *et al.*,[62] Raman spectra at ambient pressure correspond to the C-type structure, but change under pressure with new peaks emerging in the range from 400 to 500 cm^{-1} and above 600 cm^{-1} at around 15 GPa, corresponding to the B-type structure. At pressures above 25 GPa, the spectra are

Table 3 Raman peak positions of C-type Yb_2O_3 at zero pressure (ω_0) and their piezo-spectroscopic coefficients ($d\omega/dP$) compared with experimental data.

Symm.	ω_0 [cm^{-1}]			$d\omega/dP$ [cm^{-1}/GPa]	
	Calc.	Exp.[a]	Exp.[b]	Calc.	Exp.[a]
T_g	594.5	613.5	621	5.16	4.363
T_g	475.3		443	5.10	
A_g	429.9		420	4.35	
T_g	378.6	363.1	358	4.17	3.10
E_g	332.2	301.9	305	3.30	2.36
A_g	114.4		121	0.97	

[a] Pandey *et al.* [62] [b] Schaack and Koningstein [65]

Table 4 Lattice constants, bulk moduli (B_0) and formation enthalpies (ΔH_f) of Yb_2SiO_5 at zero pressure.

	X_2 phase		X_1 phase	
	Calc.	Exp.	Calc.	Exp.
a [Å]	14.328	14.37[a]	9.150	8.977[e]
b [Å]	6.697	6.693[a]	6.639	6.769[e]
c [Å]	10.323	10.34[a]	6.702	6.598[e]
β [°]	122.03	122.78[a]	101.48	105.13[e]
B_0 [GPa]	101.56	94[b]	97.35	
ΔH_f [kJ/mol]	-2677.13	-2774.75±8.21[c] -2714±11[d]	-2658.34	

[a] Anan'eva *et al.* [72] [b] Lu *et al.* [73] [c] Liang *et al.* [74] [d] Costa and Jacobson [75] [e] Wang *et al.* [71]

relatively simple, with two main peaks in the range from 450 to 550 cm^{-1}, indicating the A-type structure. The calculated spectra confirm that, for Yb_2O_3, the polymorph can be determined from the Raman spectra.

The changes in Raman spectra of C-type Yb_2O_3 as a function of pressure are shown in Fig. S1 and their gradients, viz., piezo-spectroscopic (PS) coefficients, are summarised in Table 3 and compared with experimental data.[62] The calculated PS coefficients are all larger than the experimental values. This systematic overestimation (up to about 1.4 times) may be a result of the employed exchange-correlation functional, used PAW potentials, and the absence of $4f$ electrons in the Yb valence shell.

3.2 Yb_2SiO_5

Bulk properties

In the series of R_2SiO_5, two types of phases are observed depending on the ionic radius of rare-earth element. Under ambient conditions, when the ionic radius of R is larger than that of Gd, R_2SiO_5 forms as most stable in the X_2 phase with space group $P2_1/c$, while for R with the the smaller ionic-radius, the X_2 phase with space group $C2/c$ is most stable.[9] In the latter cases, apart from Lu, R_2SiO_5, have been found as a metastable X_1 phase by sol-gel synthesis.[71] Both structures are composed of $[SiO_4]^{-4}$ units, R^{+3} ions in 6- or 7-fold coordination and isolated O^{-2} ions in the large interstices.

Calculated bulk properties of X_2 and X_1 phases of Yb_2SiO_5 are reported in Table 4. The lattice constants of both phases agree well with experimental values with differences less than 1%. The bulk modulus and formation enthalpy of the X_2 phase are also comparable with experimental results. The X_2 phase is more energetically stable than the X_1 phase by 20 kJ/mol, confirming that

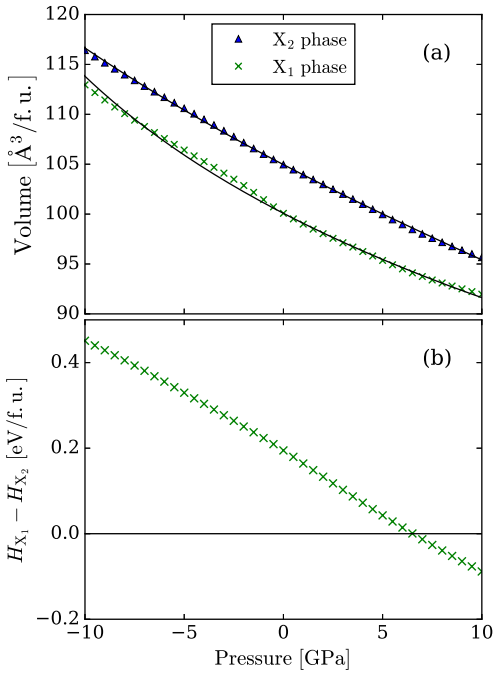

Fig. 3 Pressure dependence of (a) volume per formula unit (f.u.) of X_2- and X_1-Yb_2SiO_5, and (b) differencies in enthalpy per formula unit between the two phases.

the X_1 phase prepared by sol-gel synthesis is metastable.

The pressure dependences of volume per formula unit of X_2- and X_1-Yb_2SiO_5 and the difference in enthalpy between the two phases are plotted in Fig. 3. Figure 3(b) shows that the X_2 phase stable at zero pressure transforms to the X_1 phase under compressive pressure at around 6.5 GPa. During the transformation, the volume of Yb_2SiO_5 contracts as seen in Fig. 3(a). The behaviour is similar to that observed during pressure-induced phase transitions of other materials, e.g., Yb_2O_3 (Fig. 1).

The same pressure-induced phase transition has been reported for single-crystal $Lu_{1.8}Y_{0.2}SiO_5$ by Raman spectroscopy[27] and for Lu_2SiO_5 from DFT calculations.[76] From the Raman measurements under quasi-hydrostatic pressures, single-crystal $Lu_{1.8}Y_{0.2}SiO_5$ gradually transforms from the X_2 phase to the X_1 phase starting between around 3 GPa and 10 GPa.[27] Between these pressures, the two phases appear to coexist. DFT calculations of Lu_2SiO_5 under compressive pressure predict the transition to occur at 6.3 GPa with 3.7% volume contraction.[76] These values are close to the transition pressure of 6.5 GPa and volume contraction of 4.4% obtained for Yb_2SiO_5 in this study.

Raman spectra

The calculated Raman spectrum of X_2-Yb_2SiO_5 at zero pressure is plotted in Fig. 4(a) together with experimental data, showing that the two are in good agreement, although in the frequency range less than 300 cm^{-1} the calculated intensities are significantly weaker than the experimental ones. Table 5 lists the extracted peak positions and symmetry labels which belong

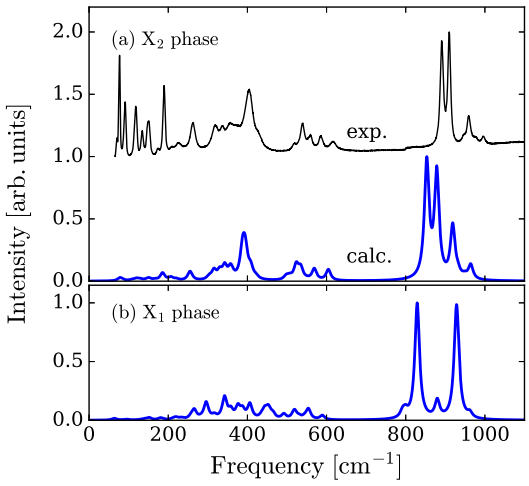

Fig. 4 Calculated Raman spectra of (a) X_2- and (b) X_1-Yb_2SiO_5, with experimental data for the X_2 phase also shown in (a).

Table 5 Raman peak positions of X_2-Yb_2SiO_5 at zero pressure (ω_0) and their piezo-spectroscopic coefficients ($d\omega/dP$) compared with experimental values.

Symm.	ω_0 [cm^{-1}]		$d\omega/dP$ [cm^{-1}/GPa]
	Calc.	Exp.	Calc.
B_g	966.7	996	7.25
A_g	921.9	959	8.38
A_g	880.2	910	5.16
A_g	855.1	891	4.73
A_g	606.3	616	4.67
B_g	570.9	540	5.10
$2A_g + B_g$	392.5	404	3.78
$A_g + B_g$	256.3	263	3.12
A_g	186.5		2.08

to $24A_g + 24B_g$ derived from point group C_{2h}^5 of the X_2 phase.[77] Because Yb^{+3} and Lu^{+3} have similar ionic radii, the Raman spectrum of Yb_2SiO_5 is expected to be comparable with the polarized Raman spectra of single-crystal Lu_2SiO_5, measured by Voron'ko *et al.*[77] From such a comparison, the symmetry labels of the two strongest intensity peaks at frequencies above 800 cm^{-1} were confirmed to be A_g. It is harder to equate directly the remaining symmetry labels from calculations of Yb_2SiO_5 in Table 5 to those from measurements of Lu_2SiO_5 with any great certainty because the frequencies of measured 24 A_g and 18 B_g modes occur close together[77] and the peak positions of calculated and experimental results sometimes differ by up to 10%.

The calculated Raman spectrum of X_1-Yb_2SiO_5 in Fig. 4(b) is similar to that of X_1-Gd_2SiO_5.[77] The spectrum exhibits two separated strong intensity peaks above 800 cm^{-1} which are different to those in the spectrum of the X_2 phase. The Raman peaks at these high frequencies, therefore, can be used to identify the structural type of Yb_2SiO_5.

Calculated changes in the Raman spectrum of X_2-Yb_2SiO_5 as a function of pressure are plotted in Fig. S2, and the peak positions and symmetry labels of Raman-active modes are summarised in Table 5. The high-frequency Raman peaks above 800 cm^{-1} indicate that X_2-Yb_2SiO_5 should have relatively large PS coefficients. Ricci *et al.* reported the pressure dependence of Raman spectra of

Table 6 Lattice constants, bulk moduli (B_0) and formation enthalpies (ΔH_f) of $Yb_2Si_2O_7$ at zero pressure.

	β phase Calc.	Exp.	γ phase Calc.	X phase Calc.	α phase Calc.
a [Å]	6.793	6.801[a]	4.742	6.602	6.570
b [Å]	8.907	8.875[a]	10.696		6.605
c [Å]	4.765	4.707[a]	5.534	12.04	12.035
α [°]					93.81
β [°]	102.21	101.84[a]	96.29		92.18
γ [°]					92.65
B_0 [GPa]	147.01	141[b]	141.28	155.78	106.88
ΔH_f	-3523.73		-3519.77	-3504.32	-3478.96

[a] Zhao *et al.* [79] [b] Tian *et al.* [80]

the X_2 phase of $Lu_{1.8}Y_{0.2}SiO_5$, extracting PS coefficients between 6.0 and 10.7 cm^{-1}/GPa from the high-frequency peaks.[27] These values span our calculated values for X_2-Yb_2SiO_5.

3.3 $Yb_2Si_2O_7$

Bulk properties

Phase diagrams of $R_2Si_2O_7$ under ambient pressure contain seven polymorphs and are more complex than those of R_2O_3 and R_2SiO_5 compounds.[10] In the case of $Yb_2Si_2O_7$, the β phase (space group $C2/m$) is stable over a wide temperature range. Studies on the effect of thermal treatment under pressures up to 7 GPa on the crystal structures of $Yb_2Si_2O_7$ have revealed that the monoclinic γ phase with space group $P2_1/c$, tetragonal X phase with space group $P4$, and triclinic α phase with space group $P\bar{1}$ appear on the T-P diagrams.[78] While the β, γ and X phases are composed of $[Si_2O_7]^{-6}$ units, the α phase contains two types of Si-O units, viz., $[Si_3O_{10}]^{-8}$ and $[SiO_4]^{-4}$. In all cases, Yb^{+3} ions are coordinated to 6 or more O.

Calculated bulk properties of the four $Yb_2Si_2O_7$ polymorphs are summarised in Table 6. Experimental values for the β phase are also shown, and found to be in good agreement with the calculated values. The stability sequence of the polymorphs at zero pressure is $\beta > \gamma > X > \alpha$. Th bulk modulus of the α phase is smaller than the other three phases and comparable to the values of Yb_2SiO_5 in Table 4. The smaller value may be attributed to the difference in the types of Si_xO_y units because only the α phase contains isolated SiO_4 units.

The pressure dependence of volume per formula unit of the four $Yb_2Si_2O_7$ phases, and differences in enthalpy per formula unit of γ, X, and α phases relative to the β phase, are plotted in Fig. 5. As the pressure increases two phase transformations occur, first from the β phase to the X phase at around 3.7 GPa, and then from the X phase to the α phase at around 16.4 GPa. Although the enthalpy of the γ phase is near to that of the β phase at zero pressure, there is no region over which the γ phase is stable because the enthalpies of the X and α phases depend more strongly on pressure than that of the γ phase. The similarity in pressure dependence of the enthalpies and volumes of the γ and β phases reflects the similarities in crystal structures of the two phases.[10]

The experimental T-P diagram[78] shows that, in the temperature range from 900 to 1250 °C, the phase sequence with increasing pressure is $\beta \rightarrow \gamma \rightarrow X \rightarrow \alpha$. On the other hand, below T = 900 °C, the β phase appears to transform directly to the X phase. At low temperature, the transition pressures for β-X and X-γ transitions are estimated to be below 2 GPa and above 6 GPa, respectively; calculated values at zero kelvin of 3.7 GPa and 16.4 GPa, respectively, are relatively large compared to the transition pressures estimated from the experimental T-P diagram.

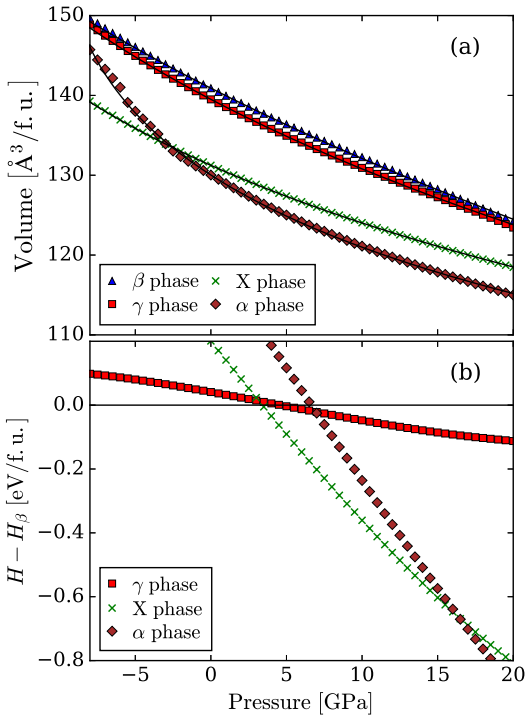

Fig. 5 Pressure dependence of (a) volume per formula unit (f.u.) of β, γ, X and α phases of $Yb_2Si_2O_7$ and (b) differences in enthalpy per formula unit between the four phases.

Raman spectra

Measured and calculated Raman spectra of β-$Yb_2Si_2O_7$ at zero pressure are plotted in Fig. 6(a). The extracted peak positions for the β phase are listed in Table 7 with symmetries belonging to $3A_{1g} + A_{2g} + 4E_g$ derived from point group C_{2h}^3 of β-$Yb_2Si_2O_7$[81]. The extracted frequencies from the experimental spectrum coincide well with results from polarized Raman spectroscopy of single-crystal β-$Yb_2Si_2O_7$ by Bretheau-Raynal *et al.*[82] Although there are differences between the calculated and experimental peak positions (around 10% or less), we can match the calculated peaks to the experimental counterparts based on symmetry.[82]

Calculated Raman spectra of the γ, X and α phases of $Yb_2Si_2O_7$ are plotted in Fig. 6(b), (c), and (d), respectively. While there are large differences between spectra of the β phase and the X and α phases over the whole frequency range, the spectrum of the γ phase is similar to that of the β phase. The structure of the γ phase could be identified by the splitting of the dual high-intensity peaks above 800 cm^{-1} because the calculated splitting values are

Table 7 Raman peak positions of β-$Yb_2Si_2O_7$ at zero pressure (ω_0), and their piezospectroscopic coefficients ($d\omega/dP$) compared with experimental values.

Symm.	ω_0 [cm^{-1}]			$d\omega/dP$ [cm^{-1}/GPa]
	Calc.	Exp.	Exp.[a]	Calc.
A_g	910.4	952	952	6.99
A_g+B_g	888.1	922	923	6.54
A_g	643.9	668	669	2.10
B_g	499.3	521	521	2.77
A_g	466.5		424	0.17
A_g	416.5	412	413	4.95
B_g	394.6			5.02
B_g	348.8	360	362	5.29
A_g	271.3	276	277	1.85
B_g	195.0		203	-1.45
A_g	145.5	144	145	0.07

[a] Bretheau-Raynal *et al.* [82]

about 22 cm^{-1} for the β phase and 35 cm^{-1} for the γ phase. A similar tendency was found for the β and γ phases of $Y_2Si_2O_7$ from DFT calculations.[83]

Dependence of the Raman spectrum of β-$Yb_2Si_2O_7$ on pressures is shown in Fig. S3, and PS coefficients of each peak are listed in Table 7. The two peaks in the high frequency range above 800 cm^{-1} exhibit large PS coefficients of about 6.5-7.0 cm^{-1}/GPa. These are smaller than the two largest PS coefficients of X_2-Yb_2SiO_5.

4 Discussion

Although the shapes of the calculated Raman spectra are similar to available data obtained experimentally, there are differences in peak positions at around 10% or less, and the calculated PS coefficients tend to be overestimated. Similar trends were obtained using alternative GGA functionals such as PBEsol[84] and AM05.[85] Similar differences in Raman frequencies between experimental and DFT have also been reported for simple molecules such as H_2O and CH_4.[29]

The calculated PS coefficients of X_2-Yb_2SiO_5 and β-$Yb_2Si_2O_7$ are 6.5-8.5 cm^{-1}/GPa in the frequency range above 800 cm^{-1}. In the case of YSZ, the PS coefficients are on the order of 1-2 cm^{-1}/GPa under uniaxial stress, which corresponds to about 3-6 cm^{-1}/GPa under hydrostatic pressure.[28] We thus expect that PS coefficients for Yb silicates are similar in magnitude to those of YSZ, suggesting that it should be possible to use Raman microscopy to measure internal stresses or pressures in the silicates.

Phonon density of states calculations of the different phases revealed no soft modes, suggesting that the materials can exist in metastable forms after release of the external pressure. This also suggests that the phase transitions occurring over a wide pressure range multiple phases can coexist. For example, the metastability of B-type Yb_2O_3 is well known.[51] However, this behaviour may vary with R because, in the case of Lu_2SiO_5, a reversible pressure-induced transition between the X_2 and X_1 phases has been observed,[27] consistent with a report that the metastable X_1 phase was not been formed when prepared by sol-gel synthesis.[71]

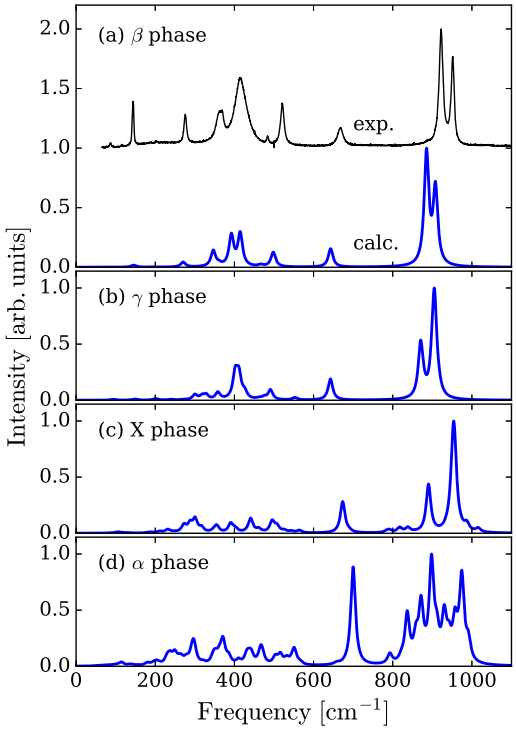

Fig. 6 Calculated Raman spectra of (a) β, (b) γ, (c) X and (d) α phases of $Yb_2Si_2O_7$, with experimental data for the β phase also shown.

Normal mode analysis

We used the inverse participation ratio (IPR) to examine locality of vibrational modes. IPR is defined by

$$\mathrm{IPR} = \frac{\sum_i (\boldsymbol{u}_i^4)}{(\sum_i \boldsymbol{u}_i^2)^2}, \quad (1)$$

where $\boldsymbol{u}_i$ is the normal-mode vector of atom i (i=1-N_{atoms}). IPRs vary from $1/N_{\mathrm{atoms}}$ for homogeneous vibrational vectors to 1 for localised ones. We also examined contributions of each element to the IPR by individuating the terms in the numerator (Eq. 1). IPRs were calculated for all vibrational modes at the Γ point.

IPRs of C-type Yb_2O_3 are plotted in Fig. 7(a). This plot shows that, while the vibrations with frequencies below 250 cm^{-1} are localised on Yb atoms, vibrations in the higher frequency range are mainly localised on O atoms. Similar conclusions were drawn from experimental Raman spectra of R_2O_3.[69] Frequencies of Raman peaks of R_2O_3 in the frequency range above 300 cm^{-1} were found to change linearly with the lattice constant because the free space for O atoms changed with the lattice constant. On the other hand, below 300 cm^{-1}, the frequencies of Raman peaks are almost independent of lattice constant because the effect of the change in lattice constant is balanced by that from the change in mass of R.

IPRs of X_2-Yb_2SiO_5 and β-$Yb_2Si_2O_7$ are shown in Fig. 7(b) and (c), respectively. In both cases, vibrations with frequencies below 200 cm^{-1} are localised on Yb atoms, similar to the case of

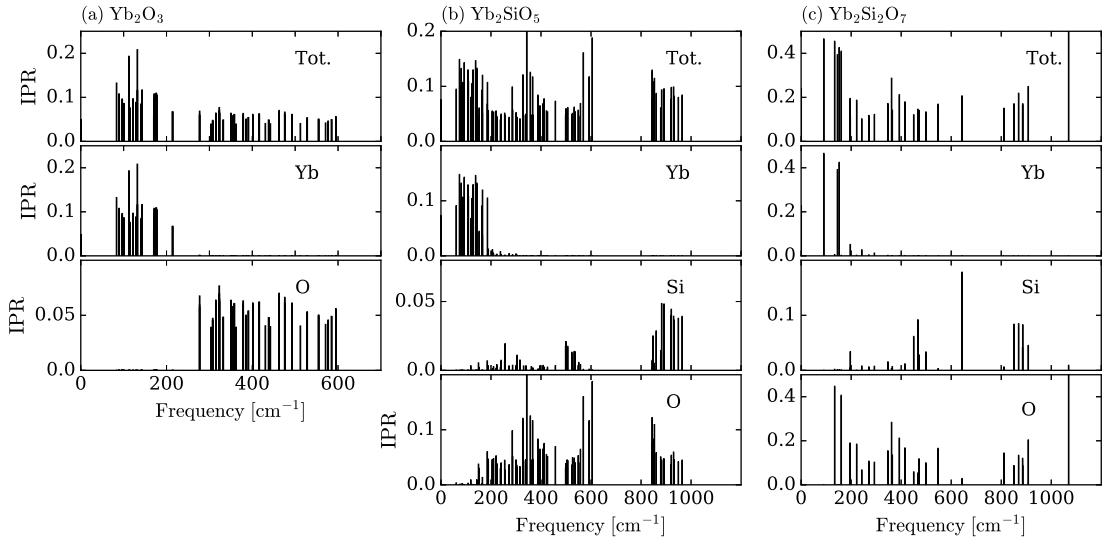

Fig. 7 Inverse participation ratios (IPRs) of (a) C-type Yb_2O_3, (b) X_2-Yb_2SiO_5 and (c) β-$Yb_2Si_2O_7$, where contributions of each element are also plotted separately.

Yb_2O_3. On the other hand, the higher-frequency modes include a large vibrational contribution from Si and O atoms. In the frequency range above 800 cm^{-1}, high-intensity IPRs for Si and O indicate that the vibrations are localised in Si-O bonds of Si_xO_y units. Since peak intensities in this frequency range are relatively large, it may be possible to use these modes as fingerprints to identify the structure, as described in the previous sections.

Vibrational modes of Si_xO_y units

Here we analyse vibrations in Si_xO_y units in Yb silicates in terms of vibrational amplitudes of atoms and maximum deviations in bond lengths from the vibrational vectors of Raman-active modes. The vibrational amplitude of the i-th atom was defined as $\boldsymbol{u}_i^2/A^2$, where A is the norm of the mode vector, given by $A = (\sum_i \boldsymbol{u}_i^2)^{1/2}$. Maximum bond-length deviations were compared using a normalised parameter, Δl_{ij}, defined as

$$\Delta l_{ij} = \frac{r_{ij}^2 - r_{ij}^{0\,2}}{r_{ij}^0 A}, \qquad (2)$$

where r_{ij}^0 and r_{ij} are bond lengths between the i-th and j-th atoms in the ground state and at maximum vibrational displacement, respectively (see the ESI). Structures of Si_xO_y units and $\boldsymbol{u}_i^2/A^2$ and Δl_{ij} values for characteristic Raman modes in the frequency range above 600 cm^{-1} for the Yb silicates are summarised in Figs. S5 – S10 of the ESI.

Vibrational characteristics of slightly distorted SiO_4 tetrahedrons in X_2- and X_1-Yb_2SiO_5 corresponding to the strong-intensity peaks at frequencies above 800 cm^{-1} are shown in Figs. S5 and S6, respectively. These modes mainly involve stretching of one or two Si-O bonds. This corresponds to asymmetric stretching vibrations (ν_3) of the free SiO_4 tetrahedron with T_d symmetry.[86] Although SiO_4 units in the X_2 phase are near to the ideal tetrahedron, two Si-O bonds in SiO_4 units of the X_1 phase are longer by about 0.04 Å than the other two bonds. These longer bonds cause softer and lower-frequency modes as shown in Fig. S6. The different amounts of separation between the strong-intensity dual peaks in the high-frequency range of the two phases can thus be explained in terms of differences in Si-O structural units between the X_2 and X_1 phases.

Vibrational characteristics of Si_2O_7 units in β-, γ- and X-$Yb_2Si_2O_7$ are illustrated in Figs. S7, S8 and S9, respectively. The Raman peaks in these systems are of two types: (A) isolated peaks at around 650 cm^{-1}, and (B) strong-intensity peaks above 800 cm^{-1}. The type-A peaks correspond to Si-O-Si stretching vibrations around an O atom bridging two SiO_4 tetrahedrons. No such peaks appear in the Yb_2SiO_5 spectra because the SiO_4 units are isolated in these structures. Positions of type-A peaks in the β and γ forms of $Yb_2Si_2O_7$ are identical, but differ from that of the X phase. This difference is caused by the bending of Si-O-Si linkages to about 140° in the X phase compared to 180° in the β and γ phases. Type-B peaks correspond to asymmetric vibrations of terminal Si-O bonds in Si_2O_7 units, as suggested by Voron'ko *et al.* in the case of $Lu_2Si_2O_7$,[81] and their vibrational motions are similar to those in SiO_4 units in Yb_2SiO_5. Precise peak positions and shapes of such asymmetric vibrations depend on the particular structure of each Si_xO_y unit and the atomic coordination environments in each crystal.

Vibrational characteristics of Si_3O_{10} and SiO_4 units in α-$Yb_2Si_2O_7$ are plotted in Fig. S10. The isolated peak at 700 cm^{-1} corresponds to Si-O-Si stretching in the Si_3O_{10} unit, similar to the type-A peaks of the Si_2O_7 unit. Although the shapes of the high-frequency Raman peaks above 800 cm^{-1} for the α phase are complex compared to those of the other silicates, analysis of vibrational vectors confirmed that the modes correspond to asymmetric stretching of Si-O bonds. These complex vibrations are a direct result of the complex crystal structures, as seen in the bond length deviations in the Si_3O_{10} unit listed in Table S1.

5 Conclusion

Phase stabilities and Raman spectra of Yb_2O_3, Yb_2SiO_5, and $Yb_2Si_2O_7$ polymorphs have been investigated based on DFT calculations, focusing on the effects of hydrostatic pressure. The sequence of phase transitions with increasing compressive pressure is consistent with available experimental data (C-type $\rightarrow$ B-type $\rightarrow$ A-type for Yb_2O_3, $X_2 \rightarrow X_1$ for Yb_2SiO_5 and $\beta \rightarrow X \rightarrow \alpha$ for $Yb_2Si_2O_7$). Spectra of polymorphs at zero pressure suggest that Raman spectroscopy can be used to identify polymorphs of these materials. From vibrational mode analyses using IPRs, vibrational amplitudes, and maximum bond-length deviations, it was found that the characteristic strong-intensity Raman peaks of Yb silicates in the frequency range above 800 cm^{-1} correspond to asymmetric vibrations in part of the Si_xO_y tetrahedral-type units. In contrast, the isolated Raman peaks observed for $Yb_2Si_2O_7$ polymorphs correspond to vibrations in Si-O-Si connections, between two SiO_4 tetrahedrons. Although PS coefficients derived from the dependence of Raman peak positions on hydrostatic pressure are overestimated for C-type Yb_2O_3 compared to experimental data, the calculated PS coefficients of X_2-Yb_2SiO_5 and β-$Yb_2Si_2O_7$ in the high-frequency range above 800 cm^{-1} are sufficiently large and of a similar order to those of YSZ so that it should be possible to use Raman microscopy to measure stress or pressure distributions in these silicates.

Acknowledgments

This work was partially supported by Cross-ministerial Strategic Innovation Promotion Program (SIP) “Structural Materials for Innovation” of the Council for Science, Technology and Innovation (SCTI) of the Japan Science and Technology Agency (JST), and by Grants-in-Aid for Scientific Research on Innovative Areas “Nano Informatics" (25106008) and KAKENHI (15K18218) from the Japan Society for the Promotion of Science (JSPS).

References

1 R. Naslain, *Compos. Sci. Technol.*, 2004, **64**, 155–170.
2 F. W. Zok, *Am. Ceram. Soc. Bull.*, 2016, **95**, 22–28.
3 K. N. Lee, *Surf. Coat. Technol.*, 2000, **133–134**, 1–7.
4 K. N. Lee, in *The Gas Turbine Handbook*, ed. R. Dennis, United States Department of Energy (DOE), 2006, ch. 4.2.2.
5 K. N. Lee, D. S. Fox and N. P. Bansal, *J. Eur. Ceram. Soc.*, 2005, **25**, 1705–1715.
6 N. Maier, K. G. Nickel and G. Rixecher, *J. Eur. Ceram. Soc.*, 2007, **27**, 2705–2713.
7 N. A. Nasiri, N. Patra, D. Horlait, D. D. Jayaseelan and W. E. Lee, *J. Am. Ceram. Soc.*, 2016, **99**, 589–596.
8 Y. Xu, X. Hu, F. Xu and K. Li, *Ceram. Int.*, 2017, **43**, 5847–5855.
9 J. Felsche, in *Rare Earths. Structure and Bonding*, ed. J. D. Dunitz, P. Hemmerich, J. A. Ibers, C. K. Jorgensen, J. B. Neilands, S. R. S. Nyholm, D. Reinen and R. J. P. Williams, Springer, Berlin, Heidelberg, 1973, vol. 13, pp. 99–197.
10 J. Felsche, *J. Less-Common Met.*, 1970, **21**, 1–14.
11 S. Ueno, T. Ohji and H.-T. Lin, *Corros. Sci.*, 2008, **50**, 178–182.
12 H. Chen, Y. Gao, Y. Liu and H. Luo, *Inorg. Chem.*, 2010, **49**, 1942–1936.
13 H. Klemm, *J. Am. Ceram. Soc.*, 2010, **93**, 1501–1522.
14 B. T. Richards, M. R. Begley and H. N. G. Wadley, *J. Am. Ceram. Soc.*, 2015, **98**, 4066–4075.
15 B. T. Richards, K. A. Young, F. de Francqueville, S. Sehr, M. R. Begley and H. N. G. Wadley, *Acta Mater.*, 2016, **106**, 1–14.
16 B. T. Richards, S. Sehr, F. de Franqueville, M. R. Begley and H. N. G. Wadley, *Acta Mater.*, 2016, **103**, 448–460.
17 X. Zhong, Y. Niu, H. Li, Y. Zeng, X. Zheng, C. Ding and J. Sun, *J. Am. Ceram. Soc.*, 2017, **100**, 1896–1906.
18 P. J. Withers and H. K. D. H. Bhadeshia, *Mater. Sci. Technol.*, 2001, **17**, 355–365.
19 N. S. Rossini, M. Dassisti, K. Y. Benyounis and A. G. Olabi, *Mater. Des.*, 2012, **35**, 572–588.
20 R. A. Forman, G. J. Piermarini, J. D. Barnett and S. Block, *Science*, 1972, **176**, 284–285.
21 Q. Ma and D. R. Clarke, *J. Am. Ceram. Soc.*, 1994, **77**, 298–302.
22 C. A. Michaels and R. F. Cook, *Mater. Des.*, 2016, **107**, 478–490.
23 V. Teixeira, M. Andritschky, W. Fischer, H. P. Buchkremer and D. Stöver, *J. Mater. Process. Technol.*, 1999, **92–93**, 209–216.
24 M. Tanaka, M. Hasegawa, A. F. Dericioglu and Y. Kagawa, *Mater. Sci. Eng., A*, 2006, **419**, 262–268.
25 K. Knipe, A. Manero II, S. F. Siddiqui, C. Meid, J. Wischek, J. Okasinski, J. Almer, A. M. Karlsson, M. Bartsch and S. Raghavan, *Nat. Commun.*, 2014, **5**, 4559.
26 C. Li, S. D. M. Jacques, Y. Chen, P. Xiao, A. M. Beale, M. di Michiel, N. Markossan, P. Nylan and R. J. Cernik, *Scripta Mater.*, 2016, **113**, 122–126.
27 P. C. Ricci, D. Chiriu, C. M. Carbonaro, S. Desgreniers, E. Fortin and A. Anedda, *J. Raman Spectrosc.*, 2008, **39**, 1268–1275.
28 A. M. Limarga and D. R. Clarke, *J. Am. Ceram. Soc.*, 2007, **90**, 1272–1275.
29 D. Porezag and M. R. Pederson, *Phys. Rev. B*, 1996, **54**, 7830–7836.
30 M. Veithen, X. Gonze and P. Ghosez, *Phys. Rev. B*, 2005, **71**, 125107.
31 Z. S. Khan, B. Zou, W. Huang, X. Fan, L. Gu, X. Chen, S. Zeng, C. Wang and X. Cao, *Mater. Sci. Eng. B*, 2012, **177**, 184–189.
32 P. E. Blöchl, *Phys. Rev. B*, 1994, **50**, 17953–17979.
33 J. P. Perdew, K. Burke and M. Ernzerhof, *Phys. Rev. Lett.*, 1996, **77**, 3865–3868.
34 G. Kresse and J. Furthmüller, *Comput. Mater. Sci.*, 1996, **6**, 15–50.
35 G. Kresse and J. Furthmüller, *Phys. Rev. B*, 1996, **54**, 11169–11186.
36 G. Kresse and D. Joubert, *Phys. Rev. B*, 1999, **59**, 1758–1775.
37 H. Jiang, P. Rinke and M. Scheffler, *Phys. Rev. B*, 2012, **86**, 125115.
38 R. Gillen, S. J. Clark and J. Robertson, *Phys. Rev. B*, 2013, **87**,

125116.
39 T. Ogawa, S. Kobayashi, M. Wada, C. A. J. Fisher, A. Kuwabara, T. Kato, M. Yoshiya, S. Kitaoka and H. Moriwake, *Phys. Rev. B*, 2016, **93**, 201107.
40 H. J. Monkhorst and J. D. Pack, *Phys. Rev. B*, 1976, **13**, 5188–5192.
41 F. Birch, *J. Geophys. Res.: Solid Earth*, 1978, **83**, 1257–1268.
42 F. Birch, *Phys. Rev.*, 1947, **71**, 809–824.
43 A. Togo and I. Tanaka, *Scripta Mater.*, 2015, **108**, 1–5.
44 M. Cardona, in *Light Scattering in Solids* II*: Basic Concepts and Instrumentation*, ed. M. Cardona and G. Güntherodt, Springer, New York, 1982, pp. 19–168.
45 A. Fonari and S. Stauffer, *vasp_raman.py*, https://github.com/raman-sc/VASP/, 2013.
46 S. Baroni, S. de Gironcoli, A. D. Corso and P. Giannozzi, *Rev. Mod. Phys.*, 2001, **73**, 515–562.
47 T. Yokoi, N. Yamaguchi, M. Tanaka, D. Yokoe, T. Kato, S. Kitaoka and M. Takata, *Mater. Lett.*, 2017, **193**, 176–178.
48 G. Adachi and N. Imanaka, *Chem. Rev.*, 1998, **98**, 1479–1514.
49 M. Zinkevich, *Prog. Mater. Sci.*, 2007, **52**, 597–647.
50 H. R. Hoekstra and K. A. Gingerich, *Science*, 1964, **146**, 1163–1164.
51 H. R. Hoekstra, *Inorg. Chem.*, 1966, **5**, 754–757.
52 A. Saiki, N. Ishizawa, N. Mizutani and M. Kato, *J. Ceram. Soc. Jpn.*, 1985, **93**, 649–654.
53 B. R. Powell, O. Hunter and W. R. Manning, *J. Am. Ceram. Soc.*, 1971, **54**, 488–490.
54 H. Yusa, T. Kikegawa and T. Tsuchiya, *Photon Factory Report 2009 Part B*, 2010, **27**, 195.
55 C. Meyer, J. P. Sanchez, J. Thomasson and J. P. Itié, *Phys. Rev. B*, 1995, **51**, 12187–12193.
56 R. J. M. Konings, O. Beneš, A. Kovács, D. Manara, D. Sedmidubský, L. Gorokhov, V. S. Iorish, V. Yungman, E. Shenyavskaya and E. Osina, *J. Phys. Chem. Ref. Data*, 2014, **43**, 013101.
57 E. J. Huber, E. L. Head and C. E. Holley, *J. Phys. Chem.*, 1956, **60**, 1457–1458.
58 E. H. P. Cordfunke and R. J. M. Konings, *Thermochim. Acta*, 2001, **375**, 51–64.
59 D. Richard, L. A. Errico and M. Renteria, *J. Alloys Compd.*, 2016, **664**, 580–589.
60 R. G. Munro, *J. Res. Natl. Inst. Stand. Technol.*, 2004, **109**, 497–503.
61 D. Lonappan, *PhD thesis*, Anna Univ. (India), 2011.
62 S. D. Pandey, K. Samanta, J. Singh, N. D. Sharma and A. K. Bandyopadhyay, *AIP Adv.*, 2013, **3**, 122123.
63 N. D. Sharma, J. Singh, A. Vijay, K. Samanta, S. Dogra and A. K. Bandyopadhyay, *J. Phys. Chem. C*, 2016, **120**, 11679–11689.
64 J. P. McClure, *PhD thesis*, University of Nevada (Las Vegas, U.S.A.), 2009.
65 G. Schaack and J. A. Koningstein, *J. Opt. Soc. Am.*, 1970, **60**, 1110–1115.
66 W. B. White and V. G. Keramidas, *Spectrochim. Acta, Part A*, 1972, **28**, 501–509.
67 N. D. Todorov, M. V. Abrashev, V. Marinova, M. Kadiyski, L. Dimowa and E. Faulques, *Phys. Rev. B*, 2013, **87**, 104301.
68 Y. Repelin, C. Proust, E. Husson and J. M. Beny, *J. Solid State Chem.*, 1995, **118**, 163–169.
69 M. V. Abrashev, N. D. Todorov and J. Geshev, *J. Appl. Phys.*, 2014, **116**, 103508.
70 M. W. Urban and B. C. Cornilsen, *J. Phys. Chem. Solids*, 1987, **48**, 475–479.
71 J. Wang, S. Tian, G. Li, F. Liao and X. Jing, *Mater. Res. Bull.*, 2001, **36**, 1855–1861.
72 G. V. Anan'eva, A. M. Korovkin, T. I. Merkulyaeva, A. M. Morozova, M. V. Petrov, I. R. Savinova, V. R. Startsev and P. P. Feofilov, *Inorg. Mater.*, 1981, **17**, 754–758.
73 M.-H. Lu, H.-M. Xiang, Z.-H. Feng, X.-Y. Wang and Y.-C. Zhou, *J. Am. Ceram. Soc.*, 2016, **99**, 1404–1411.
74 J.-J. Liang, A. Navrotsky, T. Ludwig, H. J. Seifert and F. Aldinger, *J. Mater. Res.*, 1999, **14**, 1181–1185.
75 G. C. C. Costa and N. S. Jacobson, *J. Eur. Ceram. Soc.*, 2015, **35**, 4259–4267.
76 J. Zhu, M. Gu, X. Liu, B. Liu, S. Huang and C. Ni, *Opt. Mater.*, 2013, **35**, 1659–1663.
77 Y. K. Voron'ko, A. A. Sobol, V. E. Shukshin, A. I. Zagumennyi, Y. D. Zavartsev and S. A. Koutovoi, *Opt. Mater.*, 2011, **33**, 1331–1337.
78 G. Bocquillon, C. Chateau, C. Loriers and J. Loriers, *J. Solid State Chem.*, 1977, **20**, 135–141.
79 C. Zhao, F. Wang, Y. Sun and Y. Zhou, *Ceram. Int.*, 2013, **39**, 5805–5811.
80 Z. Tian, L. Zheng, Z. Li, J. Li and J. Wang, *J. Eur. Ceram. Soc.*, 2016, **36**, 2813–2823.
81 Y. K. Voron'ko, A. A. Sobol', V. E. Shukshin and Y. V. Gerasimov, *Phys. Solid State*, 2015, **57**, 1424–1430.
82 F. Bretheau-Raynal, J. P. Dalbiez, M. Drifford and B. Blanzat, *J. Raman Spectrosc.*, 1979, **8**, 39–42.
83 R. Kaindl, D. M. Többens and V. Kahlenberg, *J. Raman Spectrosc.*, 2011, **42**, 78–85.
84 J. P. Perdew, A. Ruzsinszky, G. I. Csonka, O. A. Vydrov, G. E. Scuseria, L. A. Constantin, X. Zhou and K. Burke, *Phys. Rev. Lett.*, 2008, **100**, 136406.
85 R. Armiento and A. E. Mattsson, *Phys. Rev. B*, 2005, **72**, 085108.
86 S. P. S. Porto and J. F. Scott, *Phys. Rev.*, 1967, **157**, 716–719.